# Early Jurassic Mafic Intrusions in the Southern Youjiang Basin, SW China: Petrogenesis, Tectonic and Metallogenic Implications

**Wen Jiang [1]** [iD]**, Quanren Yan [1],\*, Li Deng [1], Bin Zhou [1], Zhongjin Xiang [2] and Wenjing Xia [3]**

[1] College of Earth and Planetary Sciences, University of Chinese Academy of Sciences, Beijing 100049, China; jahnwen@126.com (W.J.); dengli18@mails.ucas.ac.cn (L.D.); zhoubin17@mails.ucas.ac.cn (B.Z.)

[2] Institute of Geology of Chinese Academy of Geological Sciences, Beijing 100037, China; zhjxiang@cags.ac.cn

[3] Department of Student Affairs, Beihang University, Beijing 100191, China; xiawenjing89@163.com

\* Correspondence: qryan@ucas.edu.cn; Tel.: +86-10-8825-6907

![check for updates]

**Abstract:** A suite of mafic intrusions, composed of diabase and micro-gabbro outcrops in the Jingxi area of southern Youjiang Basin, SW China. This study conducts geochronological, geochemical, and Sr–Nd isotopic analyses on the mafic intrusions in Jingxi with the aim of determining their petrogenesis, tectonic setting, and metallogenic implications. Zircon U–Pb dating for the mafic intrusions yielded an age of $183 \pm 3$ Ma (MSWD = 2.3), which is coeval with the Carlin-like gold mineralization in the Youjiang Basin. The mafic intrusions are alkaline in composition and characterized by low $TiO_2$ (1.25–1.87 wt %) contents and low Ti/Y ratios (410–550). They exhibit OIB-like patterns of trace element distribution and they have low $(^{87}Sr/^{86}Sr)_i$ ratios of 0.704341 to 0.705677, slightly negative $\varepsilon_{Nd}(t)$ values of −0.30 to −2.16, low La/Ta (11.57–15.66) and La/Nb (0.77–1.06) ratios, with $[La/Yb]_N = 6.52$–10.63. The geochemical characteristics, combined with regional considerations, suggest that the mafic intrusions originated from partial melting of upwelling asthenosphere within the garnet-spinel transition zone, as a result of intracontinental back-arc extension triggered by the steep subduction of the Paleo-Pacific plate beneath the South China Block. Moreover, the new data not only suggest Early Jurassic magma was a possible heat source, but also support a magmatism-related model for the Carlin-like gold mineralization in the Youjiang Basin.

**Keywords:** mafic rock; Carlin-like gold deposits; Youjiang Basin; intracontinental back-arc extension; geochemistry

## 1. Introduction

Mafic magmas originate from the partial melting of the upper mantle, recording the nature of the mantle source. The geochemical composition and crystallization age of mafic rocks, in this regard, can be used to analyze deep geodynamic processes and regional tectonic setting. At the same time, mafic magmas may also carry ore-forming elements and drive ore-forming hydrothermal fluid circulation. Mafic rocks, therefore, can also provide important information to understand regional metallogenesis.

The Youjiang Basin (also known as Nanpanjiang Basin) is located in the southwest margin of the South China Block (SCB), and the sporadically exposed magmatic rocks in the basin are dominated by mafic rocks (Figure 1). Previous studies have focused on the Late Paleozoic-Triassic mafic rocks [1–7], while the Late Mesozoic magmatic rocks, especially the Jurassic mafic rocks, were rarely reported. Moreover, little attention has been paid to the Late Mesozoic tectonics of the Youjiang Basin, leading to the tectonic setting of the area being unclear [8]. In addition, the Youjiang Basin is known as the "Dian-Qian-Gui Golden Triangle" region, where the Carlin-like gold deposits are widely developed

(Figure 1b) [8–15]. The field crosscutting relationships suggest that the Carlin-like gold mineralization took place between Early Jurassic and Late Cretaceous [13,15]. Furthermore, it has been interpreted that the gold mineralization was associated with deep magmatism, either the ore-forming fluid originated from a magmatic source [12,13,16], or the magma heated meteoric water and drove hydrothermal fluid to extract ore-forming elements from sedimentary rocks [9]. However, outcropping igneous rocks that are coeval with the gold mineralization in the Youjiang Basin has rarely been found, and the thermal event for the gold mineralization remains poorly understood [8]. Therefore, the identification and study of a Late Mesozoic mafic rock in the Youjiang Basin should provide significant clues to analyze the Late Mesozoic tectonics and the thermal driver of the Carlin-like gold mineralization in the area.
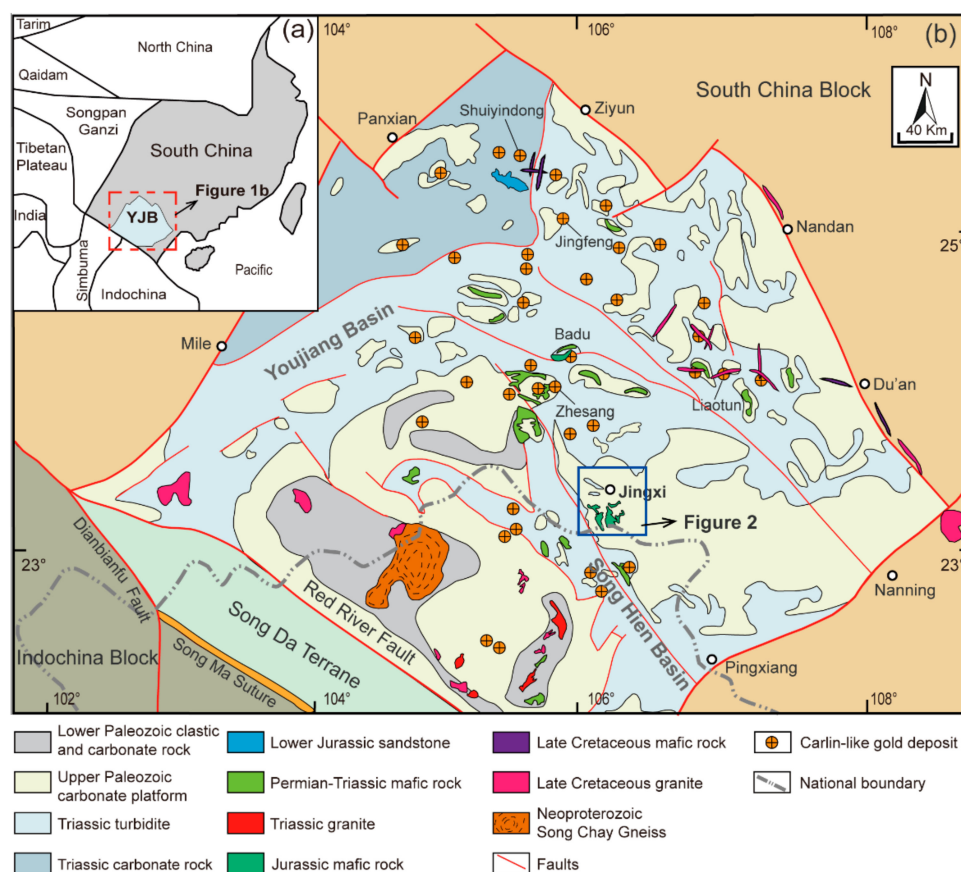


**Figure 1.** (**a**) Tectonic framework of East Asia (revised after [17]). (**b**) Simplified regional geological map of the Youjiang Basin and adjacent areas (after [10,18]) and 1:500,000 geological map of central South China made by the Chinese Academy of Geological Sciences in 2012). YJB = Youjiang Basin.

In this paper, the Early Jurassic mafic intrusions were newly identified in the Jingxi area of the southern Youjiang Basin (western Guangxi Province, SW China). We have conducted a study of LA-ICP-MS zircon U–Pb dating, whole-rock major and trace elements and Sr–Nd isotopes for the mafic intrusions in the Jingxi area. These data are used to constrain their emplacement age and to explore their petrogenesis and tectonic setting, and they probably shed new light on the Late Mesozoic tectonic evolution and the Carlin-like gold mineralization in the Youjiang Basin.

## 2. Geological Setting and Petrography

The Youjiang Basin is bound by the Mile-Shizhong-Panxian fault to the northwest, Ziyun-Nandan-Du'an fault to the northeast, Pingxiang-Nanning Fault to the southeast, and extends southward to connect with Song Hien Basin in northeastern Vietnam (Figure 1b). The dominantly exposed strata in the Youjiang Basin are Middle-Lower Triassic deep-marine turbidite depositions

and isolated Upper Paleozoic shallow-marine carbonate platforms (Figure 1b). A shallow-marine Lower Triassic carbonate platform developed in the northwest margin of the basin, whereas a small amount of Jurassic-Cretaceous terrestrial clastic rocks sporadically occurred in the interior of the basin (Figures 1b and 2) [19,20]. Known magmatic rocks in the Youjiang Basin are scarce. The mainly exposed magmatic rocks are Permian in age and represented by diabases, gabbros, and basalts (269–254 Ma) [1–5]. Middle Triassic basaltic andesites (241 Ma) [6], Late Triassic gabbro-norites (~215 Ma) [7], and minor Late Cretaceous alkaline ultramafic dikes (85–88 Ma) [21], as well as quartz porphyry dikes (95–97Ma) [11] are also exposed in this region. Recently, it has been suggested that the Youjiang Basin was an intracontinental back-arc basin and the sediments of Triassic turbidite deposition in the basin were derived from poorly preserved continental arc associated with the westward subduction of the Paleo-Pacific rather than the hypothesized collisional orogen between the South China and Indochina Blocks [22,23].Moreover, the Permian gabbros in the Babu area of southern Youjiang Basin were linked to the intracontinental back-arc extension related to the westward subduction of the Paleo-Pacific [24].
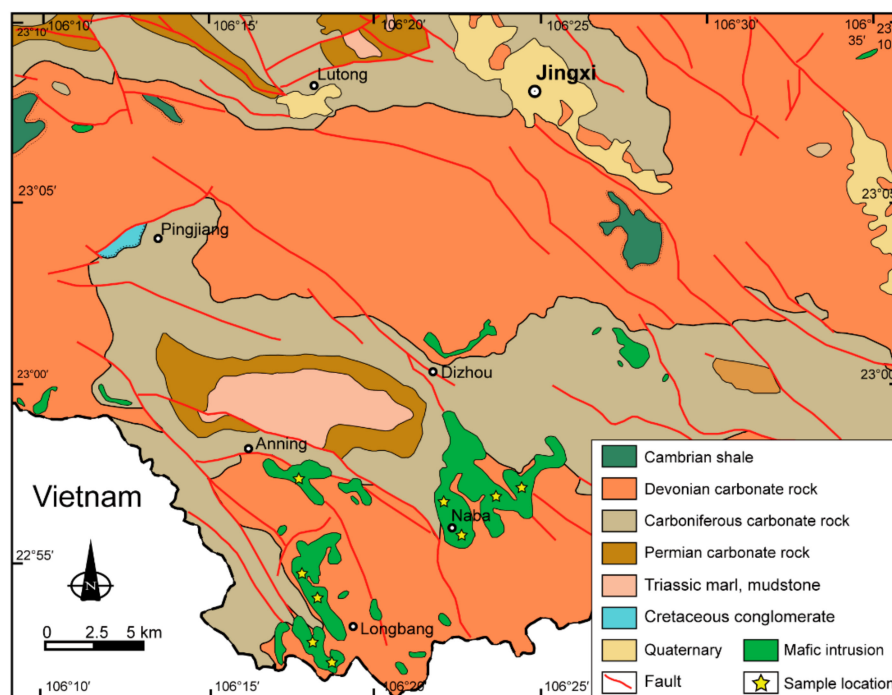


**Figure 2.** Simplified geological map of the Jingxi area (after 1:200,000 geologic map of the Jingxi sheet [25]).

The mafic intrusions in the Jingxi area of southern Youjiang Basin occur as sills, small stocks, and dikes (Figure 3a), distributing along faults (Figure 2). The mafic intrusions intruded into Devonian and Carboniferous limestones, and the limestones at the contact zone with mafic intrusions are partially metamorphosed to marbles [25]. Although the mafic intrusions in Jingxi are lacking isotopic age, they have been considered to be emplaced in Mesozoic based on the field relationships [25]. The mafic intrusions range in composition from diabase to micro-gabbro. The diabase is the main rock type, and mainly consists of plagioclase (45–50%) and clinopyroxene (35–45%) with typical diabasic texture; ilmenite and titanomagnetite are the main accessory minerals (Figure 3b–d). The micro-gabbro has similar mineral compositions with the diabase. However, compared to the diabase, the micro-gabbro mostly occurs in the center of an intrusion and has relatively coarse-grained mineral crystals, as it is exemplified by the Naba intrusion (Figure 2).
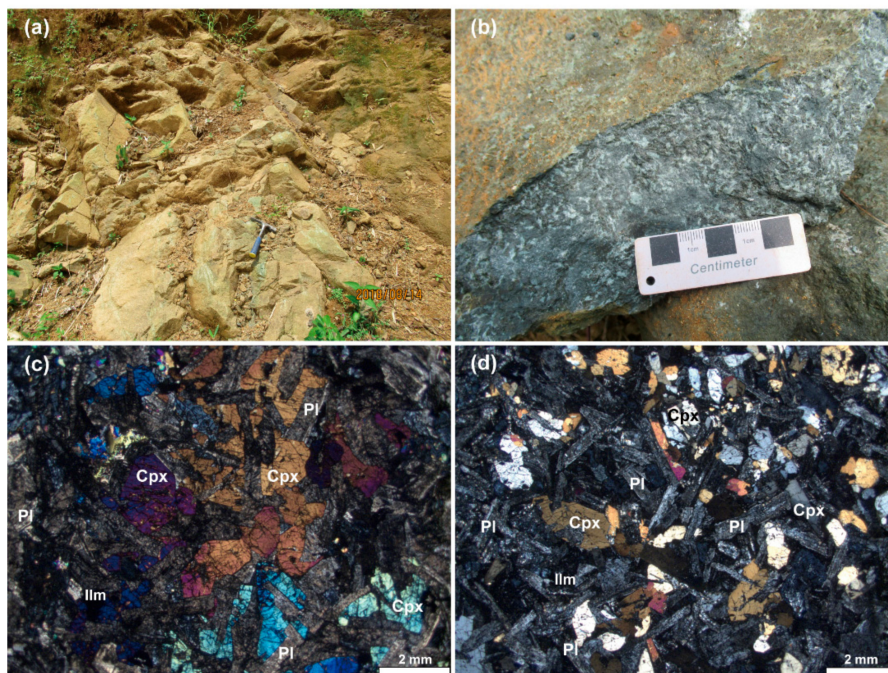
**Figure 3.** Photographs of field outcrop (**a**) and hand specimen (**b**) for the representative diabases in Jingxi. Photomicrographs showing petrographic and textural characteristics of the diabase in Jingxi (**c**,**d**). Cpx = clinopyroxene; Pl = plagioclase; Ilm = Ilmenite.

## 3. Analytical Methods

### 3.1. Zircon U–Pb Dating

Samples for zircon U–Pb dating are from coarse-grained micro-gabbros, and about 80–100 kg of rocks were collected for zircon separation. Zircon grains were separated using conventional heavy-liquid and magnetic separation techniques. Subsequently, the zircons were mounted in a diameter of 25.4 mm epoxy resin, and the zircon surfaces were polished following the mounting. Photomicrographs of transmitted and reflected light for the zircons, as well as cathodoluminescence (CL) images of the zircons, were taken for identifying the internal structures and selecting suitable positions for U–Pb isotope analysis. Zircon U–Pb isotope ratios dating was conducted at the Key Laboratory of Metallogenesis and Resource Assessment, Institute of Mineral Resources, Chinese Academy of Geological Sciences (CAGS), Beijing, China. The analyses were carried out on a Bruker M90 inductively coupled plasma-mass spectrometry (Bruker, Billerica, MA, USA) that was attached to a Resolution S155 193 nm laser ablation system (LA-ICP-MS). The laser ablation uses a beam diameter of 25 μm. The detailed operating procedures for the laser ablation and the ICP-MS system and the data processing are the same as those described by [26]. The zircon U–Pb dating results are listed in Table 1.

**Table 1.** LA-ICP-MS Zircon U–Pb dating results of the mafic intrusions in Jingxi.

| Spot | U | Pb | Th/U | $^{207}Pb/^{235}U$ | | $^{206}Pb/^{238}U$ | | Age (Ma) | | | | | | Con % |
|------|---|----|------|-----|-----|-----|-----|--------------|-----|--------------|-----|--------------|-----|-------|
| | ppm | ppm | | Ratio | 1σ | Ratio | 1σ | $^{207}Pb/^{206}Pb$ | 1σ | $^{207}Pb/^{235}U$ | 1σ | $^{206}Pb/^{238}U$ | 1σ | |
| | | | | | | | | 17Nb-1, micro-gabbro | | | | | | |
| 01 | 568 | 99 | 0.77 | 0.2083 | 0.0073 | 0.0293 | 0.0004 | 264.9 | 77.8 | 192.1 | 6.2 | 186.4 | 2.6 | 96 |
| 02 | 139 | 28 | 0.99 | 0.2117 | 0.0110 | 0.0284 | 0.0005 | 376.0 | 109 | 195.0 | 9.2 | 180.5 | 3.3 | 92 |
| 03 | 357 | 62 | 0.84 | 0.2040 | 0.0068 | 0.0278 | 0.0004 | 361.2 | 77.8 | 188.5 | 5.8 | 176.9 | 2.7 | 93 |
| 04 | 204 | 42 | 0.98 | 0.2090 | 0.0119 | 0.0278 | 0.0005 | 383.4 | 120 | 192.7 | 10.0 | 177.1 | 3.3 | 91 |
| 05 | 211 | 48 | 1.20 | 0.1982 | 0.0090 | 0.0287 | 0.0005 | 205.6 | 98.1 | 183.6 | 7.7 | 182.6 | 3.1 | 99 |
| 06 | 439 | 90 | 0.77 | 0.2675 | 0.0110 | 0.0347 | 0.0006 | 431.5 | 75.9 | 240.7 | 8.8 | 220.1 | 3.5 | 91 |
| 107 | 456 | 47 | 0.32 | 0.2602 | 0.0076 | 0.0362 | 0.0005 | 294.5 | 59.3 | 234.9 | 6.1 | 229.0 | 3.4 | 97 |
| 08 | 121 | 23 | 0.47 | 0.4319 | 0.0162 | 0.0530 | 0.0008 | 576.0 | 76.8 | 364.5 | 11.5 | 333.2 | 4.9 | 91 |
| 09 | 863 | 119 | 0.63 | 0.2154 | 0.0059 | 0.0298 | 0.0005 | 298.2 | 45.4 | 198.1 | 4.9 | 189.5 | 3.2 | 95 |
| 10 | 118 | 17 | 0.74 | 0.2120 | 0.0122 | 0.0286 | 0.0005 | 350.1 | 126 | 195.2 | 10.2 | 181.9 | 2.8 | 92 |
| 11 | 769 | 120 | 0.91 | 0.1887 | 0.0042 | 0.0278 | 0.0004 | 161.2 | 43.5 | 175.5 | 3.6 | 176.9 | 2.6 | 99 |
| 12 | 610 | 109 | 1.19 | 0.2149 | 0.0112 | 0.0288 | 0.0006 | 301.9 | 94.4 | 197.7 | 9.4 | 182.8 | 3.8 | 92 |
| 13 | 200 | 36 | 0.53 | 0.3416 | 0.0115 | 0.0474 | 0.0008 | 294.5 | 65.7 | 298.4 | 8.7 | 298.5 | 5.0 | 99 |
| 14 | 341 | 62 | 0.57 | 0.3350 | 0.0081 | 0.0454 | 0.0007 | 346.4 | 51.8 | 293.4 | 6.2 | 286.4 | 4.4 | 97 |
| 15 | 395 | 48 | 0.45 | 0.2485 | 0.0072 | 0.0352 | 0.0005 | 257.5 | 70.4 | 225.3 | 5.8 | 223.1 | 3.4 | 99 |
| 16 | 543 | 121 | 0.98 | 0.2203 | 0.0065 | 0.0292 | 0.0006 | 279.7 | 90.7 | 202.1 | 5.4 | 185.9 | 3.7 | 91 |
| 17 | 507 | 67 | 0.55 | 0.2080 | 0.0067 | 0.0296 | 0.0006 | 105.6 | 90.7 | 191.8 | 5.6 | 187.8 | 3.5 | 97 |
| 18 | 915 | 148 | 0.67 | 0.2111 | 0.0095 | 0.0282 | 0.0009 | 211.2 | 111 | 194.4 | 8.0 | 179.2 | 5.6 | 91 |
| 19 | 767 | 168 | 1.04 | 0.2079 | 0.0054 | 0.0299 | 0.0005 | 200.1 | 73.1 | 191.8 | 4.6 | 190.1 | 2.9 | 99 |
| 20 | 853 | 135 | 0.74 | 0.2073 | 0.0045 | 0.0290 | 0.0005 | 294.5 | 46.3 | 191.3 | 3.8 | 184.2 | 2.8 | 96 |
| 21 | 368 | 193 | 0.96 | 0.6043 | 0.0146 | 0.0781 | 0.0013 | 477.8 | 44.4 | 479.9 | 9.3 | 484.5 | 7.6 | 99 |
| 22 | 262 | 119 | 0.70 | 0.6918 | 0.0148 | 0.0856 | 0.0013 | 550.0 | 40.7 | 533.9 | 8.9 | 529.7 | 7.7 | 99 |
| 23 | 238 | 96 | 0.81 | 0.5385 | 0.0161 | 0.0672 | 0.0011 | 600.0 | 59.3 | 437.4 | 10.6 | 419.2 | 6.4 | 95 |
| 24 | 116 | 51 | 0.32 | 1.4241 | 0.0345 | 0.1506 | 0.0021 | 892.3 | 48.1 | 899.1 | 14.5 | 904.5 | 11.6 | 99 |
| 25 | 159 | 52 | 0.93 | 0.3492 | 0.0113 | 0.0475 | 0.0008 | 353.8 | 70.4 | 304.1 | 8.5 | 299.3 | 4.6 | 98 |
| 26 | 530 | 163 | 0.85 | 0.4025 | 0.0120 | 0.0514 | 0.0008 | 479.7 | 83.3 | 343.5 | 8.7 | 323.1 | 5.2 | 93 |
| 27 | 483 | 218 | 0.42 | 1.3083 | 0.0273 | 0.1321 | 0.0021 | 977.5 | 31.5 | 849.4 | 12.0 | 799.7 | 11.9 | 93 |
| 28 | 194 | 65 | 1.05 | 0.3141 | 0.0116 | 0.0446 | 0.0008 | 255.6 | 79.6 | 277.3 | 9.0 | 281.6 | 4.9 | 98 |
| 29 | 1379 | 490 | 1.00 | 0.4194 | 0.0092 | 0.0501 | 0.0007 | 620.4 | 35.2 | 355.6 | 6.6 | 315.1 | 4.5 | 87 |
| 30 | 203 | 128 | 0.66 | 1.1598 | 0.0251 | 0.1271 | 0.0017 | 809.3 | 40.7 | 781.9 | 11.8 | 771.5 | 9.5 | 98 |

Con = Concordance.

## 3.2. Whole-Rock Major and Trace Element and Sr–Nd Isotope Measurements

Whole-rock major and trace element analyses were performed at the National Research Center of Geoanalysis, CAGS, Beijing, China. Major element oxides were analyzed using X-ray fluorescence (XRF) with an analytical uncertainty of <0.5%. Besides, FeO (wt %) is determined by wet chemical analysis. Trace elements were determined using Inductively Coupled Plasma Mass Spectrometry (ICP-MS). The analytical uncertainties are 10% when the element abundance is <10 ppm, and around 5% when the element abundance >10 ppm. The major and trace element results are listed in Table 2.

Whole-rock Sr–Nd isotope measurements were taken at State Key Laboratory for Mineral Deposits Research, Nanjing University, Nanjing, China, following the methods similar to [27]. For Sr–Nd isotope analysis, about 150~200 mg of powder (crushed to 200 mesh) for each sample was dissolved and purified. The Sr standard NIST SRM-987 and the Nd standard JNdi-1 were used in this study, yielding an average $^{87}Sr/^{86}Sr$ ratio of 0.710224 ± 0.000007 (*n* = 4, 1sd) and $^{143}Nd/^{144}Nd$ ratio of 0.512106 ± 0.000016 (*n* = 3, 2sd), respectively. The results of Sr–Nd isotopes are shown in Table 3.

**Table 2.** Whole-rock major (wt %) and trace element (µg/g) of the mafic intrusions in Jingxi.

| Sample | 17Lb-1 | 17Lb-2 | 17Lb-3 | 17Lb-4 | 17Lb-5 | 17Lb-6 | 17Lb-7 | 17Nb-1 | 17Nb-2 | 17Nb-3 | 17Nb-4 | 17Nb-5 |
|---|---|---|---|---|---|---|---|---|---|---|---|---|
| $SiO_2$ | 48.62 | 48.00 | 47.56 | 47.54 | 48.35 | 48.58 | 48.19 | 51.11 | 53.00 | 50.94 | 52.96 | 51.14 |
| $Al_2O_3$ | 16.38 | 16.70 | 16.90 | 16.65 | 16.59 | 16.26 | 16.59 | 16.67 | 15.39 | 16.32 | 15.32 | 16.67 |
| CaO | 8.27 | 9.01 | 9.28 | 9.72 | 9.51 | 10.21 | 9.06 | 7.50 | 4.14 | 7.57 | 4.15 | 7.52 |
| $Fe_2O_3$ | 2.08 | 1.75 | 1.34 | 1.82 | 2.15 | 1.92 | 2.39 | 1.71 | 2.82 | 2.28 | 2.45 | 1.66 |
| FeO | 6.59 | 5.80 | 6.30 | 5.95 | 5.30 | 6.27 | 5.41 | 5.73 | 6.83 | 5.19 | 6.74 | 5.80 |
| $K_2O$ | 1.35 | 0.75 | 0.84 | 0.85 | 0.70 | 0.26 | 0.61 | 2.14 | 2.50 | 2.20 | 2.50 | 2.13 |
| MgO | 7.09 | 5.57 | 5.41 | 5.80 | 5.87 | 7.06 | 5.96 | 5.82 | 5.33 | 5.63 | 5.32 | 5.82 |
| MnO | 0.13 | 0.13 | 0.13 | 0.13 | 0.12 | 0.12 | 0.12 | 0.12 | 0.11 | 0.11 | 0.11 | 0.12 |
| $Na_2O$ | 3.94 | 4.91 | 4.76 | 4.47 | 4.84 | 4.05 | 4.73 | 4.02 | 5.00 | 3.98 | 5.03 | 4.04 |
| $P_2O_5$ | 0.22 | 0.26 | 0.25 | 0.24 | 0.22 | 0.23 | 0.22 | 0.25 | 0.38 | 0.28 | 0.38 | 0.26 |
| $TiO_2$ | 1.30 | 1.28 | 1.33 | 1.39 | 1.25 | 1.37 | 1.29 | 1.30 | 1.87 | 1.41 | 1.86 | 1.30 |
| LOI | 3.02 | 4.52 | 4.55 | 4.56 | 4.67 | 3.09 | 4.43 | 2.61 | 2.48 | 2.76 | 2.43 | 2.58 |
| Total | 98.99 | 98.68 | 98.65 | 99.12 | 99.57 | 99.42 | 99.00 | 98.98 | 99.85 | 98.67 | 99.25 | 99.04 |
| $Mg^{\#}$ | 0.66 | 0.63 | 0.61 | 0.64 | 0.67 | 0.67 | 0.66 | 0.65 | 0.58 | 0.66 | 0.59 | 0.64 |
| La | 13.00 | 17.00 | 15.90 | 14.10 | 14.00 | 16.60 | 16.10 | 16.60 | 27.70 | 18.90 | 28.50 | 16.30 |
| Ce | 25.40 | 31.80 | 30.50 | 27.70 | 27.10 | 29.40 | 28.30 | 31.40 | 56.60 | 35.70 | 57.00 | 31.40 |
| Pr | 3.49 | 4.38 | 4.12 | 3.75 | 3.60 | 4.71 | 4.08 | 4.17 | 6.95 | 4.70 | 7.03 | 4.10 |
| Nd | 14.80 | 18.00 | 17.00 | 15.20 | 14.50 | 19.60 | 17.20 | 17.00 | 26.30 | 18.80 | 26.90 | 16.80 |
| Sm | 3.31 | 3.88 | 3.57 | 3.42 | 3.21 | 4.41 | 3.77 | 3.66 | 5.61 | 4.02 | 5.74 | 3.62 |
| Eu | 1.26 | 1.45 | 1.42 | 1.30 | 1.26 | 1.67 | 1.48 | 1.39 | 1.89 | 1.50 | 1.98 | 1.38 |
| Gd | 3.88 | 4.40 | 4.07 | 3.77 | 3.66 | 5.16 | 4.31 | 4.12 | 6.11 | 4.55 | 6.26 | 4.10 |
| Tb | 0.57 | 0.66 | 0.62 | 0.57 | 0.56 | 0.75 | 0.65 | 0.61 | 0.89 | 0.66 | 0.91 | 0.61 |
| Dy | 3.18 | 3.58 | 3.36 | 3.13 | 3.15 | 4.25 | 3.53 | 3.25 | 4.69 | 3.60 | 4.81 | 3.29 |
| Ho | 0.68 | 0.75 | 0.69 | 0.64 | 0.65 | 0.88 | 0.73 | 0.66 | 0.96 | 0.74 | 1.00 | 0.66 |
| Er | 1.77 | 1.89 | 1.76 | 1.66 | 1.61 | 2.13 | 1.86 | 1.66 | 2.41 | 1.84 | 2.44 | 1.65 |
| Tm | 0.25 | 0.27 | 0.25 | 0.24 | 0.24 | 0.29 | 0.27 | 0.23 | 0.32 | 0.25 | 0.33 | 0.23 |
| Yb | 1.43 | 1.52 | 1.42 | 1.33 | 1.36 | 1.56 | 1.48 | 1.28 | 1.87 | 1.42 | 1.97 | 1.27 |
| Lu | 0.23 | 0.25 | 0.24 | 0.22 | 0.23 | 0.26 | 0.24 | 0.21 | 0.30 | 0.24 | 0.32 | 0.21 |
| Y | 14.50 | 16.90 | 15.20 | 14.50 | 15.10 | 19.40 | 16.80 | 15.30 | 21.30 | 16.80 | 21.10 | 14.90 |
| Sc | 20.20 | 19.50 | 19.10 | 20.50 | 21.20 | 27.30 | 22.00 | 18.50 | 17.50 | 19.20 | 17.30 | 18.10 |
| V | 172 | 151 | 161 | 174 | 146 | 194 | 158 | 161 | 166 | 163 | 170 | 159 |
| Co | 34.20 | 29.70 | 32.00 | 32.40 | 30.70 | 36.90 | 30.30 | 29.50 | 24.70 | 29.30 | 25.50 | 28.50 |

**Table 2.** *Cont.*

| Sample | 17Lb-1 | 17Lb-2 | 17Lb-3 | 17Lb-4 | 17Lb-5 | 17Lb-6 | 17Lb-7 | 17Nb-1 | 17Nb-2 | 17Nb-3 | 17Nb-4 | 17Nb-5 |
|---|---|---|---|---|---|---|---|---|---|---|---|---|
| Ni | 86.40 | 126 | 109 | 111 | 119 | 120 | 136 | 60.30 | 17.20 | 60 | 17.40 | 60.20 |
| Cu | 57.20 | 66.00 | 69.40 | 66.90 | 65.20 | 87.90 | 80.20 | 29.00 | 16.50 | 35.90 | 17.30 | 25.90 |
| Rb | 19.70 | 14.80 | 16.20 | 17.00 | 13.60 | 4.63 | 12.40 | 24.80 | 27.00 | 25.30 | 27.00 | 24.80 |
| Sr | 628 | 752 | 794 | 758 | 686 | 695 | 652 | 1038 | 346 | 1043 | 344 | 1010 |
| Zr | 85.70 | 121 | 123 | 109 | 112 | 101 | 113 | 108 | 175 | 121 | 179 | 109 |
| Nb | 14.10 | 19.90 | 19.90 | 18.40 | 18.00 | 15.70 | 18.80 | 18.20 | 30.60 | 20.60 | 31.60 | 18.00 |
| Ta | 0.96 | 1.34 | 1.34 | 1.21 | 1.21 | 1.06 | 1.25 | 1.21 | 1.99 | 1.33 | 2.05 | 1.22 |
| Ba | 307 | 593 | 695 | 481 | 496 | 544 | 470 | 445 | 485 | 452 | 488 | 447 |
| Hf | 2.47 | 3.10 | 3.04 | 2.89 | 2.88 | 2.65 | 2.92 | 2.85 | 4.41 | 3.17 | 4.60 | 2.82 |
| Pb | 2.92 | 2.20 | 5.38 | 2.19 | 1.63 | 2.72 | 2.01 | 2.00 | 3.60 | 3.78 | 3.62 | 2.02 |
| Th | 2.08 | 2.40 | 2.27 | 2.00 | 2.17 | 1.79 | 2.18 | 2.87 | 4.96 | 3.23 | 5.07 | 2.90 |
| U | 0.47 | 0.61 | 0.58 | 0.51 | 0.56 | 0.46 | 0.55 | 0.68 | 1.20 | 0.77 | 1.21 | 0.70 |
| Cr | 231 | 217 | 196 | 262 | 280 | 401 | 303 | 292 | 53.40 | 313 | 54 | 288 |
| La/Ta | 13.54 | 12.69 | 11.87 | 11.65 | 11.57 | 15.66 | 12.88 | 13.72 | 13.92 | 14.21 | 13.90 | 13.36 |
| La/Nb | 0.92 | 0.85 | 0.80 | 0.77 | 0.78 | 1.06 | 0.86 | 0.91 | 0.91 | 0.92 | 0.90 | 0.91 |
| Zr/Nb | 6.08 | 6.08 | 6.18 | 5.92 | 6.22 | 6.43 | 6.01 | 5.93 | 5.72 | 5.87 | 5.66 | 6.06 |
| Th/La | 0.16 | 0.14 | 0.14 | 0.14 | 0.16 | 0.11 | 0.14 | 0.17 | 0.18 | 0.17 | 0.18 | 0.18 |
| Nb/U | 30.00 | 32.62 | 34.31 | 36.08 | 32.14 | 34.13 | 34.18 | 26.76 | 25.50 | 26.75 | 26.12 | 25.71 |
| Ti/Y | 518 | 433 | 513 | 550 | 479 | 410 | 460 | 485 | 488 | 471 | 512 | 501 |
| [La/Yb]$_N$ | 6.52 | 8.02 | 8.03 | 7.60 | 7.38 | 7.63 | 7.80 | 9.30 | 10.63 | 9.55 | 10.38 | 9.21 |

LOI = loss on ignition. Mg# = $Mg^{2+}$ / ($Mg^{2+}$ + $Fe^{2+}$). [La/Yb]$_N$ = La/Yb ratio is normalized to chondritic values.

**Table 3.** Sr and Nd isotopic compositions of mafic intrusions in Jingxi.

| Sample | Age (Ma) | Rb (ppm) | Sr (ppm) | $^{87}Rb/^{86}Sr$ | $^{87}Sr/^{86}Sr$ | ±1$\sigma$ | $(^{87}Sr/^{86}Sr)_i$ | Sm (ppm) | Nd (ppm) | $^{147}Sm/^{144}Nd$ | $^{143}Nd/^{144}Nd$ | ±1$\sigma$ | $(^{143}Nd/^{144}Nd)_i$ | $\varepsilon_{Nd}(t)$ |
|---|---|---|---|---|---|---|---|---|---|---|---|---|---|---|
| 17Lb-1 | 183 | 19.7 | 628.0 | 0.0908 | 0.705914 | 5 | 0.705677 | 3.31 | 14.8 | 0.1352 | 0.512549 | 2 | 0.512387 | −0.30 |
| 17-Lb2 | 183 | 14.8 | 752.0 | 0.0570 | 0.705808 | 8 | 0.705660 | 3.88 | 18 | 0.1303 | 0.512528 | 2 | 0.512372 | −0.59 |
| 17Nb-1 | 183 | 24.8 | 1038.0 | 0.0692 | 0.705180 | 6 | 0.705000 | 3.66 | 17 | 0.1302 | 0.512448 | 3 | 0.512292 | −2.16 |
| 17Nb-2 | 183 | 27.0 | 346.0 | 0.2260 | 0.704929 | 6 | 0.704341 | 5.61 | 26.3 | 0.1290 | 0.512450 | 2 | 0.512295 | −2.09 |

## 4. Results

### 4.1. Zircon U–Pb Ages

The sample 17Nb-1 is a coarse-grained micro-gabbro, and 30 zircon grains of the sample has been analyzed. One zircon grain (spot 29) with concordance less than 90% was excluded from the calculation. In the remaining 29 zircon grains, the youngest group of 14 zircon grains yielded a mean $^{206}Pb/^{238}U$ age of 183 ± 3 Ma (MSWD = 2.3, Figure 4). These 14 zircon grains have Th/U ratios of 0.55–1.19, have oscillatory zones, and show similar morphologies, euhedral, ranging in length from 50 to 100 µm, suggesting magmatic origins (Figure 5). The remaining 15 zircon grains obtained older ages, ranging from 223 Ma to 905 Ma, and they show different morphologies and have a certain degree of roundness (Figure 5) consistent with inherited xenocrysts. Therefore, the youngest age of 183 ± 3 Ma is considered as the best estimate of the crystallization age.
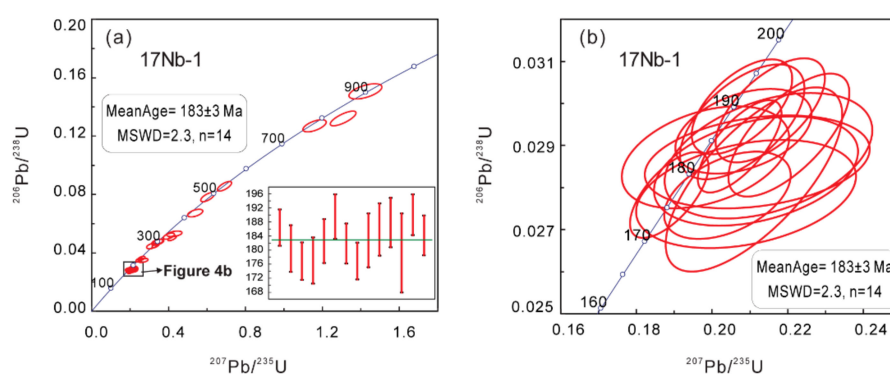


**Figure 4.** Zircon U–Pb age Concordia plots of the mafic intrusions in Jingxi.
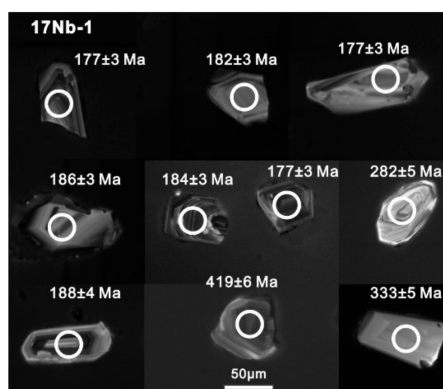


**Figure 5.** Cathodoluminescence (CL) images of representative zircons for the mafic intrusions in Jingxi.

### 4.2. Whole-Rock Geochemical Data and Sr–Nd Isotopic Compositions

All samples underwent various degrees of alteration, as shown by a relatively high loss on ignition values (LOI, 2.43–4.67 wt %). These rocks have a narrow composition of $SiO_2$ (48.00–53.00 wt %) and MgO (5.32–7.09 wt %) and are characterized by low $TiO_2$ (1.25–1.87 wt %) and Ti/Y ratios (410–550, average = 485). On the $Zr/TiO_2$ vs. Nb/Y diagram, all samples plot in the field of alkaline series (Figure 6). The mafic rocks show relatively steep REE patterns (Figure 7a), with $(La/Yb)_N$ = 6.52–10.63. On the trace element spider diagram, they show enrichment in incompatible elements (e.g., Rb, Th, and U) similar to OIB, except for higher Ba content (Figure 7b).
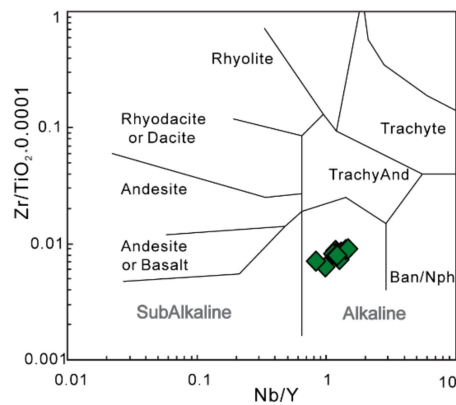
**Figure 6.** Geochemical classification of the mafic intrusions in Jingxi. The Nb/Y vs. $Zr/TiO_2 \times 0.0001$ diagram from [28].
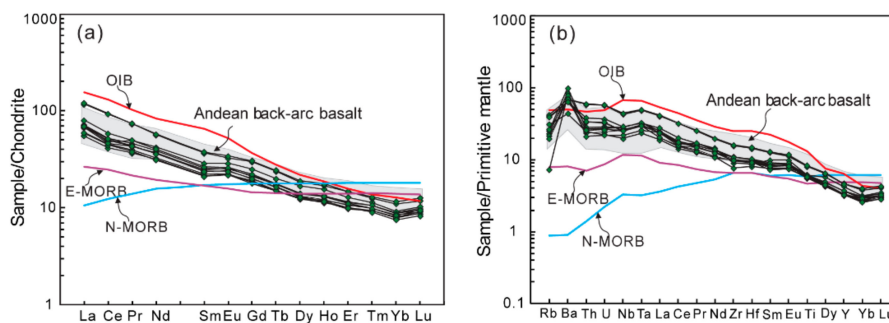


**Figure 7.** Chondrite normalized REE patterns (**a**), and primitive-mantle normalized trace spider diagrams (**b**) for the mafic intrusions in Jingxi. Normalizing values and OIB, MORB data are from [29] Andean back-arc basalts are from [30].

The mafic rocks in the Jingxi area have a narrow composition of Sr–Nd isotopes (Table 3). The initial isotopic ratios were calculated to 183 Ma. The $(^{87}Sr/^{86}Sr)_i$ ratios range from 0.704341 to 0.705677, and the $\varepsilon_{Nd}(t)$ values range from −0.30 to −2.16. In the $(^{87}Sr/^{86}Sr)_i$ versus $\varepsilon_{Nd}(t)$ correlation diagram, they show Sr–Nd isotopic compositions similar to those of OIBs and fall into the field of Early Jurassic mafic rocks in the inland of the South China Block (Figure 8).
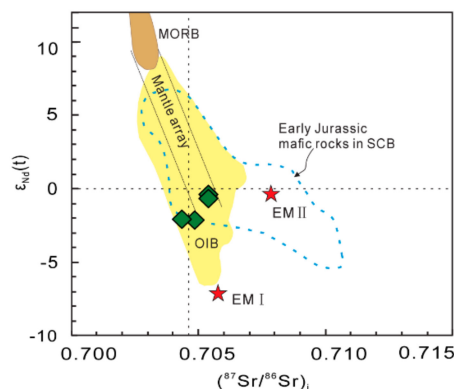


**Figure 8.** $\varepsilon_{Nd}(t)$ vs. $(^{87}Sr/^{86}Sr)_i$ diagram for the mafic intrusions in Jingxi. Data sources: OIB [31], EM I (Enriched mantle I) & EM II (Enriched mantle II) [32], MORB [33]. The Early Jurassic rocks in the inland of the South China Block are shown for comparison, data sources: [34–39].

## 5. Discussion

*5.1. Petrogenesis*

5.1.1. Effect of Alteration, Crustal Contamination, and Fractional Crystallization

The samples of mafic intrusions in Jingxi have a relatively high LOI (2.43–4.67 wt %, Table 2), and therefore it is necessary to evaluate the potential effects of alteration processes on the use of trace elements. In general, Zr is considered as the most immobile element in the low-grade alteration and metamorphism process [40]. Thus, Zr can be used as an alternation-independent index to evaluate the mobility of other elements [41,42]. The high field strength elements (HFSE, e.g., Nb, Ta, Hf, and Ti), REE, Y, Th, and U are significantly correlated with Zr (online Supplementary File, Figure S1), which suggests that these elements were basically immobile during the alteration [42]. It is also supported by the uniform variations of these trace elements (HSFE, REE, Y, Th, and U) on the trace element spider diagram (Figure 7). Therefore, alteration had an insignificant effect on the HFSE, REE, Y, Th, and U of the samples, and the following discussions mainly focus on these immobile elements.

For the mafic intrusions in Jingxi, the inherited zircons and slightly enriched Sr–Nd isotopic compositions imply some degree of crustal contamination. However, the lack of clear correlation between Nb/La and $SiO_2$, MgO (Figure 9a,b) argues against extensive crustal contamination, since crust contamination would decrease Nb/La ratios, resulting in a negative correlation between Nb/La ratios and $SiO_2$, and a positive correlation between Nb/La ratios and MgO. Moreover, the Sr–Nd isotopic compositions for the samples do not clearly correlate with increasing $SiO_2$ and decreasing MgO contents (Figure 9c,d), suggesting insignificant crustal contamination. They have much lower Th/Nb (0.06–0.12) and Th/Ce (0.02–0.06) ratios, but a much higher Nb/U (25.5–36.08) ratio than the upper continental crust (Th/Nb = 0.86, Th/Ce = 0.17, Nb/U = 4.4, [43]. These geochemical signatures are inconsistent with extensive crustal contamination. Thus, we suggest that crustal contamination played an insignificant role during magma ascent, and the enriched Sr–Nd isotopic signatures mainly resulted from source enrichment.
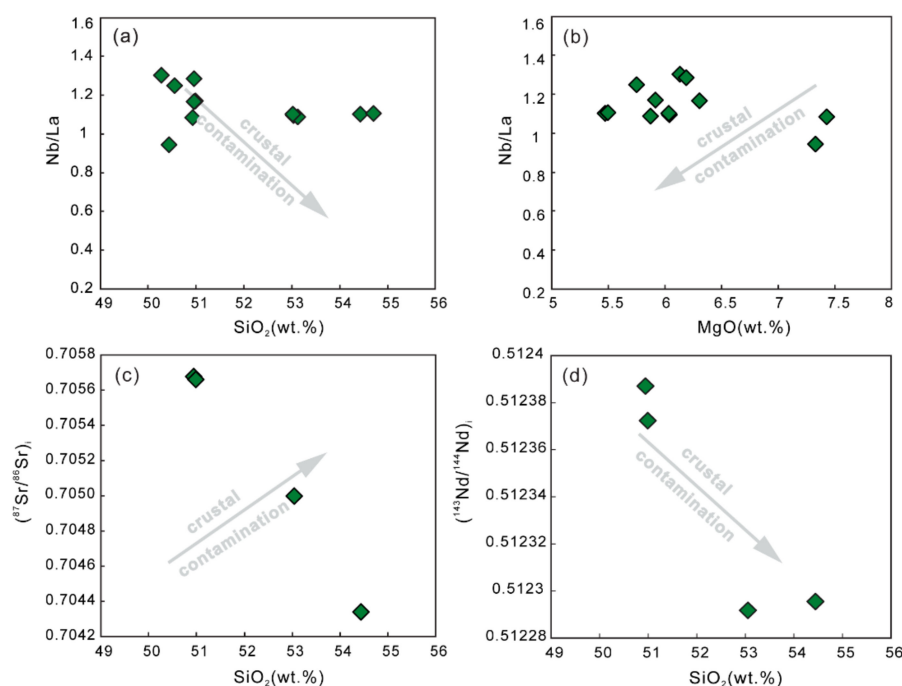


**Figure 9.** Plots of the mafic intrusions in Jingxi. (**a**) $SiO_2$ vs. Nb/La; (**b**) MgO vs. Nb/La; (**c**) $SiO_2$ vs. $(^{87}Sr/^{86}Sr)_i$; (**d**) $SiO_2$ vs. $(^{143}Nd/^{144}Nd)_i$. All major oxides are normalized to 100% on a volatile-free basis.

All the basaltic magmas from the Jingxi mafic intrusions are not primary mantle melt as shown by their low Mg# (0.58–0.67), MgO (5.32–7.06 wt %), Ni (17.2–120 ppm), and Cr (53.4–313 ppm) contents. These characteristics suggest that they have experienced a variable degree of fractional crystallization from parent magmas. The negative correlations of MgO, $TFe_2O_3$, CaO, and $Al_2O_3$ vs. $SiO_2$, and negative correlations of Cr and Ni contents vs. MgO (Figure 10), presumably imply the fractionation of olivine and/or clinopyroxene. In contrast, they show an increase of $P_2O_5$ and $TiO_2$ with the increasing $SiO_2$ (Figure 10e,f), which might reflect insignificant fractionation of apatite and Ti–Fe oxides. The weakly positive Eu anomaly ($\delta Eu$ = 1.01–1.12) probably suggests minor accumulation of plagioclase.
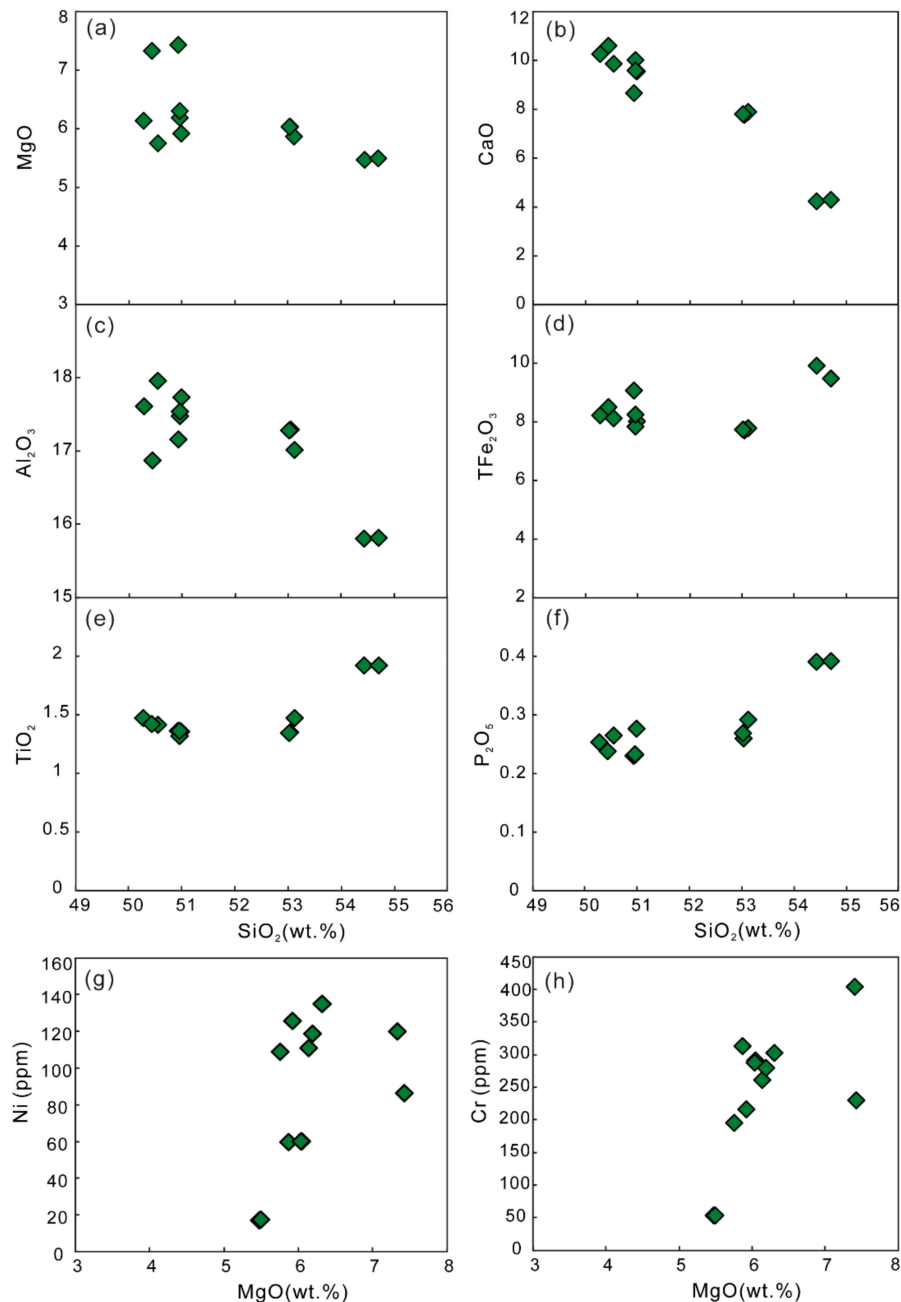


**Figure 10.** Harker diagrams for the mafic intrusion in Jingxi. (**a**) $SiO_2$ vs. MgO; (**b**) $SiO_2$ vs. CaO; (**c**) $SiO_2$ vs. $Al_2O_3$; (**d**) $SiO_2$ vs. $TFe_2O_3$ (Total Fe); (**e**) $SiO_2$ vs.$TiO_2$; (**f**) $SiO_2$ vs. $P_2O_5$; (**g**) MgO vs. Ni; (**h**) MgO vs. Cr. All major oxides are normalized to 100% on a volatile-free basis.

### 5.1.2. Origin of the Mafic Intrusions in Jingxi

The mafic intrusions in Jingxi have intraplate-like low La/Ta (11.57–14.21), La/Nb (0.77–1.06), Zr/Nb (5.72–6.43), and Th/La (0.11–0.18) ratios and high Nb/U (25.50–36.08) ratios, and these ratios fall near or within the range of OIB [29,44,45]. Moreover, they exhibit REE and trace element patterns similar to OIB (Figure 7). The low ($^{87}$Sr/$^{86}$Sr)$_i$ ratios (0.704341–0.705677) and slightly negative $\varepsilon_{Nd}(t)$ values (−0.30 to −2.16) of the Jingxi mafic rocks probably suggest that they derived from a weakly enriched mantle source. They show low La/Ta ratios (11.57–15.66, i.e., <30) and La/Nb ratios (0.77–1.06, i.e., <1.5) similar to the values observed from the asthenospheric mantle and much lower than those basalts from the lithospheric mantle [46,47], which suggests that they resulted from an asthenospheric mantle. Generally, high [La/Yb]$_N$ ratios reflect mantle melting dominated by relatively small melting fractions and/or garnet as the predominant residual phase (thick lithosphere), whereas low [La/Yb]$_N$ ratios correspond to larger melting fractions and/or spinel control (thin lithosphere, [48]). The Jingxi mafic intrusions show low [La/Yb]$_N$ ratios (6.52–10.63), which implies the spinel is a residual phase. The plot of Sm/Yb vs. La/Sm can effectively distinguish between the melting of spinel-and garnet-lherzolite sources. When a spinel-lherzolite undergoes partial melting, Sm/Yb ratios of the melt are nearly unfractionated, while La/Sm ratios decrease with increasing degree of partial melting. In contrast, Sm/Yb ratios will strongly fractionate during the small (or moderate) degree of partial melting of a garnet-lherzolite source [49,50]. Therefore, partial melting of a spinel-lherzolite source will generate a nearly horizontal melting trend, while a partial melting of a garnet-lherzolite source will create a steep melting trend to higher Sm/Yb ratios on the Sm/Yb against La/Sm plot [49]. The mafic rocks in Jingxi have a steep Sm/Yb melting trend but fall below the garnet-lherzolite melting curves (Figure. 11), and the Sm/Yb-La/Sm systematics also cannot be explained by the partial melting of a spinel-lherzolite source. Thus, the simplest model to explain the Sm/Yb-La/Sm systematics of the mafic rocks in Jingxi is the partial melting of lherzolite in the garnet-spinel transition zone. Furthermore, Figure 11 shows a 3–6% non-model batch melting of a hypothetical light REE-enriched garnet-spinel lherzolite ([La/Yb]$_N$ > 1) can generate the Sm/Yb-La/Sm systematics of the Jingxi mafic rocks.
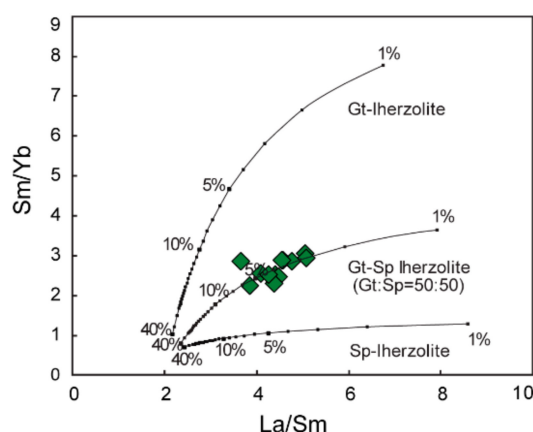


**Figure 11.** A plot of Sm/Yb vs. La/Sm for the mafic intrusions in Jingxi. The shown melt curve of spinel lherzolite and garnet lherzolite are calculated using non-modal batch melting equations of [51]. Numbers along melting curves are the degree of partial melting. Spinel- and garnet-lherzolite models are from [52]. Partition coefficients are taken from the GERM Partition Coefficient Database.

### 5.2. Tectonic Implications

The OIB-like mafic rocks are usually linked to mantle plume [31,53] or tectonic extension of the continental lithosphere, and the latter may include: (1) lithospheric delamination triggered by gravity instability during post-orogenic stage [54,55]; and (2) intracontinental back-arc extension [30,56]. Zircon U–Pb isotopic data indicate that the mafic intrusions in Jingxi emplaced at 183 ± 3 Ma (Figure 4), which is consistent with the newly reported zircon U–Pb age of Badu diabase in the middle Youjiang

Basin (187 ± 3 Ma [57], suggesting that Early Jurassic magmatism occurred in this region. In SW China, the mantle plume activity took place in Middle Permian (Emeishan plume, ~260 Ma, [58,59]), and therefore the Early Jurassic mafic rocks in Jingxi cannot be associated with the Emeishan mantle plume due to the large age gap. A post-orogenic lithospheric delamination tectonic setting would trigger widespread magmatism of diverse compositions, including basaltic rocks with intraplate geochemical characteristics, bimodal magmatism and A-type granites [55,60,61]. However, the delamination mechanism can be excluded due to the limited magmatism and the lack of contemporaneous granitic rocks in the Youjiang Basin and adjacent areas during Early Jurassic. Instead, the mafic rocks in Jingxi exhibit REE patterns and trace spider diagrams similar to the modern back-arc basalts in the Andes (Figure 7), and they are also plotted in the back-arc field on the tectonic discrimination diagrams (Figure 12). Therefore, the mafic intrusions in Jingxi most likely formed at an intracontinental back-arc tectonic setting analogous to the modern Andean back-arc basalts.
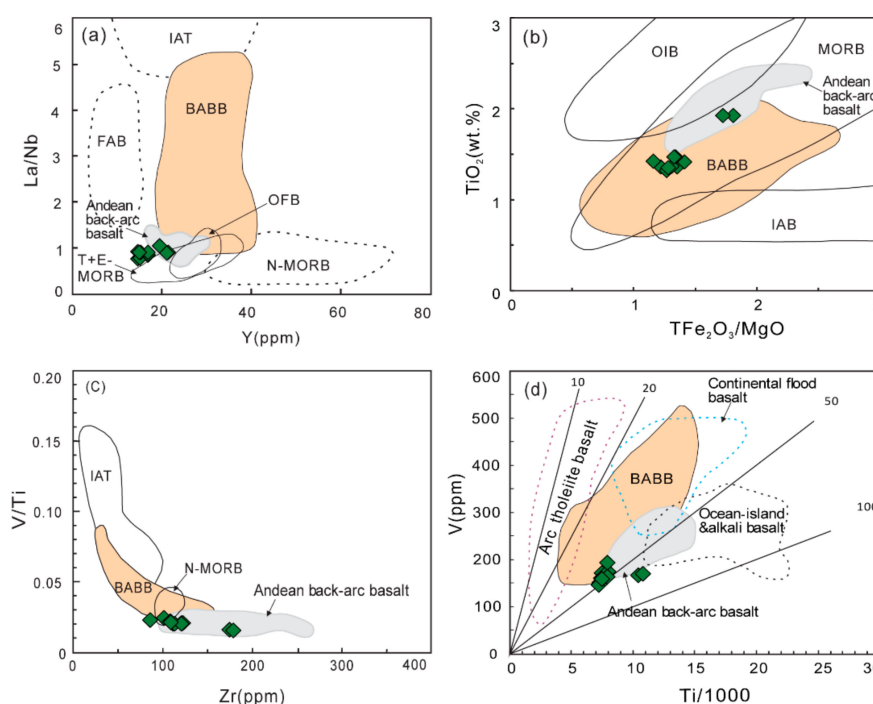


**Figure 12.** Tectonic discrimination diagrams for the mafic intrusions in Jingxi. (**a**) Y vs. La/Nb [62]; (**b**) TFe$_2$O$_3$ vs. TiO$_2$ [63]; (**c**) Zr vs. V/Ti [64]; (**d**) Ti/1000 vs.V [65]. Andean back-arc basalts are from [30]. BABB = Back-arc basin basalt; FAB = Fore-arc basalt; IAB = Island arc basalt; IAT = Island arc tholeiites; OFB = Ocean floor basalt.

It has been suggested that the subduction of the Paleo-Pacific plate beneath the South China Block occurred from the Permian [66,67], and the Permian gabbros in the Badu area of southern Youjiang Basin were linked to the back-arc extension [24]. Additionally, the Youjiang Basin is thought to be an extensional continental back-arc basin associated with the westward subduction of the Paleo-Pacific during Triassic [22,23]. The newly drilled Early Jurassic arc-related granites and diorites from NE South China Sea and SW East China Sea [68,69], combined with Talun granite in SE Taiwan [70], define a NE-SW trending Dongsha-Talun-Yandang magmatic arc zone along the eastern margin of the SCB [68,69]. The identified Jurassic accretionary complexes in Southwest Japan, the Ryukyu Islands, Taiwan, and West Philippines [71–74] are paired with this magmatic arc zone in response to the subduction of the Paleo-Pacific slab beneath the SCB [68]. In this case, a corresponding back-arc extension regime probably occurred in the inland Youjiang Basin during the Early Jurassic. Accordingly, the Jingxi mafic intrusions show OIB-like trace elements characteristics and have an intracontinental back-arc extensional setting, which is consistent with such a geodynamic model. Therefore, we suggest

that the Youjiang Basin was under the tectonic setting of intracontinental back-arc extension caused by the steep subduction of the Paleo-Pacific plate beneath the SCB during the Early Jurassic (Figure 13).
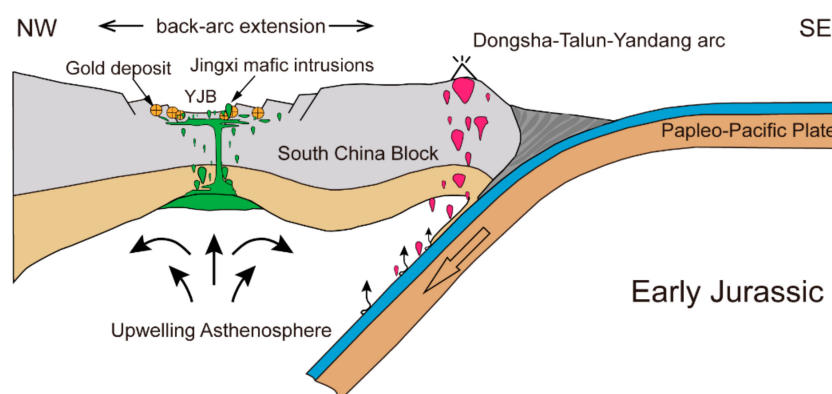


**Figure 13.** Tectonic model for the intracontinental back-arc extensional origin of the Jingxi mafic intrusions and the formation of the Carlin-like gold deposits in the Youjiang Basin, SW China. YJB = Youjiang Basin.

*5.3. Implications for the Carlin-like Gold Mineralization in the Youjiang Basin*

Although the exact age of the Carlin-like gold mineralization in the Youjiang Basin remains controversial as the age of the gold mineralization is difficult to date directly, the proposed age based on field crosscutting relationships is thought to be the most reliable [13,15]. Some of the orebodies in the Shuiyingdong and Jingfeng gold deposits crosscut the folds consisted of Early Jurassic strata [13,15], while some of the orebodies in the Liaotun gold deposit were crosscut by Late Cretaceous (ca. 95 Ma) felsic dikes (Figure 1b, [11]). These field relationships indicate that the Carlin-like gold deposits in the Youjiang Basin formed between Early Jurassic and Late Cretaceous [13]. Consistent with these crosscutting relationships, various hydrothermal minerals isotopic dating data constrain the age of the gold mineralization to a wide range between 193 Ma and 141 Ma [10,18,75,76]. As mentioned above, the gold mineralization in the Youjiang Basin has long been considered to be related to the deep magmatism, either the ore-forming elements derived from magma or the ore-forming hydrothermal fluid was driven by magma [9,12,13,16]. However, no contemporaneous igneous outcrops in the Youjiang Basin have been found before. Our newly identified Early Jurassic mafic intrusions in the Jingxi area emplaced at 183 ± 3 Ma, which is contemporaneous with the time of the gold mineralization. Such Early Jurassic magma was a probable heat source to drive hydrothermal fluids for the generation of the Carlin-like gold deposits, and it supports the magmatism-related metallogenic model [9,12,13,16]. In addition, the Early Jurassic magmatism in the southern Youjiang Basin was formed at an intracontinental back-arc extensional setting. Therefore, we propose that the metallogenic setting of the Carlin-like gold deposits in the Youjiang Basin is the same intracontinental back-arc extensional regime (Figure 13), which is analogous to Carlin-type gold deposits in Nevada [77,78].

## 6. Conclusions

(1) The mafic intrusions in the Jingxi area emplaced at 183 ± 3 Ma, which suggests the discovery of an Early Jurassic magmatic event in the southern Youjiang Basin.

(2) The mafic intrusions in the Jingxi area have OIB-like geochemical characteristics, and magmas of these mafic rocks derived from partial melting of upwelling asthenosphere within the garnet-spinel transition zone, were as a result of the intracontinental back-arc extension caused by the steep subduction of the Paleo-Pacific plate beneath the South China Block.

(3) Early Jurassic magmatism was a probable heat source for the formation of the Carlin-like gold deposits in the Youjiang Basin, and it supported a metallogenic setting of intracontinental back-arc extension and a magmatism-related metallogenic model.

## References

1. Fan, W.M.; Zhang, C.H.; Wang, Y.J.; Guo, F.; Peng, T.P. Geochronology and geochemistry of Permian basalts in western Guangxi Province, Southwest China: Evidence for plume-lithosphere interaction. *Lithos* **2008**, *102*, 218–236. [CrossRef]

2. Zhou, M.F.; Zhao, J.H.; Qi, L.; Su, W.C.; Hu, R.Z. Zircon U–Pb geochronology and elemental and Sr–Nd isotope geochemistry of Permian mafic rocks in the Funing area, SW China. *Contrib. Mineral. Petrol.* **2006**, *151*, 1–19. [CrossRef]

3. Xia, W.J.; Yan, Q.R.; Xiang, Z.J.; Xia, L.; Jiang, W.; Li, X.J.; Zhou, B.; Deng, L. Baddeleyite and Zircon U–Pb Dating of Badu Diabase in the Nanpanjiang Basin and Its Tectonic Significance. *Acta Geosci. Sin.* **2019**, *40*, 265–278. (In Chinese)

4. Fan, W.M.; Wang, Y.J.; Peng, T.P.; Miao, L.C.; Guo, F. Ar–Ar and U–Pb geochronology of Late Paleozoic basalts in western Guangxi and its constraints on the eruption age of Emeishan basalt magmatism. *Chin. Sci. Bull.* **2004**, *49*, 2318–2327. (In Chinese) [CrossRef]

5. Zhang, B.H.; Ding, J.; Zhang, L.K.; Zhang, B.; Chen, M.H. SHRIMP zircon U–Pb Chronology of the Badu Ophiolite in Southern Yunnan Province. *Acta Geol. Sin.* **2013**, *87*, 1498–1509. (In Chinese)

6. Hu, L.S.; Du, Y.S.; Yang, J.H.; Huang, H.; Huang, H.W.; Huang, Z.Q. Geochemistry and tectonic significance of middle Triassic volcanic rocks in Nalong, Guangxi area. *Geol. Rev.* **2012**, *58*, 481–494. (In Chinese)

7. Pi, Q.H.; Hu, R.Z.; Peng, K.Q.; Wu, J.B.; Wei, Z.W.; Huang, Y. Geochronology of the Zhesang gold deposit and mafic rock in Funing Country of Yunnan Province, with special reference to dynamic background of Calin-type gold deposits in the Dian-Qian-Gui region. *Acta Petrol. Sin.* **2016**, *32*, 3331–3342. (In Chinese)

8. Wang, Q.F.; Groves, D. Carlin-style gold deposits, Youjiang Basin, China: Tectono-thermal and structural analogues of the Carlin-type gold deposits, Nevada, USA. *Min. Depos.* **2018**, *53*, 909–918. [CrossRef]

9. Hu, R.; Fu, S.; Yong, H.; Zhou, M.F.; Fu, S.; Zhao, C.; Wang, Y.; Bi, X.; Xiao, J. The giant South China Mesozoic low-temperature metallogenic domain: Reviews and a new geodynamic model. *J. Asian Earth Sci.* **2017**, *137*, 9–34. [CrossRef]

10. Chen, M.H.; Bagas, L.; Liao, X.; Zhang, Z.Q.; Li, Q.L. Hydrothermal apatite SIMS Th Pb dating: Constraints on the timing of low-temperature hydrothermal Au deposits in Nibao, SW China. *Lithos* **2019**, *324*, 418–428. [CrossRef]

11. Zhu, J.J.; Hu, R.Z.; Richards, J.P.; Bi, X.W.; Stern, R.; Lu, G. No genetic link between Late Cretaceous felsic dikes and Carlin-type Au deposits in the Youjiang basin, Southwest China. *Ore Geol. Rev.* **2017**, *84*, 328–337. [CrossRef]

12. Zhang, Y.; Xia, Y.; Su, W.C.; Tao, Y.; Zhang, X.C.; Liu, J.Z.; Deng, Y.M. Metallogenic model and prognosis of the Shuiyindong super-large strata-bound Carlin-type gold deposit, southwestern Guizhou Province, China. *Chin. J. Geochem.* **2010**, *29*, 157–166. [CrossRef]

13. Xie, Z.; Xia, Y.; Cline, J.S.; Pribil, M.J.; Koenig, A.; Tan, Q.; Wei, D.; Wang, Z.; Yan, J. Magmatic Origin for Sediment-Hosted Au Deposits, Guizhou Province, China: In Situ Chemistry and Sulfur Isotope Composition of Pyrites, Shuiyindong and Jinfeng Deposits. *Econ. Geol.* **2018**, *113*, 1627–1652. [CrossRef]

14. Tan, Q.; Xia, Y.; Xie, Z.; Wang, Z.; Wei, D.; Zhao, Y.; Yan, J.; Li, S. Two Hydrothermal Events at the Shuiyindong Carlin-Type Gold Deposit in Southwestern China: Insight from Sm–Nd Dating of Fluorite and Calcite. *Minerals* **2019**, *9*, 230. [CrossRef]

15. Su, W.; Dong, W.; Zhang, X.; Shen, N.; Hu, R.; Hofstra, A.H.; Cheng, L.; Xia, Y.; Yang, K. Carlin-Type Gold Deposits in the Dian-Qian-Gui "Golden Triangle" of Southwest China. *Rev. Econ. Geol.* **2018**, *20*, 157–185.

16. Yan, J.; Hu, R.Z.; Liu, S.; Lin, Y.T.; Zhang, J.C.; Fu, S.L. NanoSIMS element mapping and sulfur isotope analysis of Au-bearing pyrite from Lannigou Carlin-type Au deposit in SW China: New insights into the origin and evolution of Au-bearing fluids. *Ore Geol. Rev.* **2018**, *92*, 29–41. [CrossRef]

17. Metcalfe, I. Paleozoic and Mesozoic tectonic evolution and palaeogeography of East Asian crustal fragments: The Korean Peninsula in context. *Gondwana Res* **2006**, *9*, 24–46. [CrossRef]

18. Nevolko, P.A.; Trong Hoa, T.; Yudin, D.S.; Thi Phuong, N. Ar-Ar ages of gold deposits in the Song Hien domain (NE Vietnam): Tectonic settings and comparison with Golden Triangle in China in terms of a single metallogenic province. *Ore Geol. Rev.* **2017**, *89*, 544–556. [CrossRef]

19. Wang, Z.S. Affrmation of the Jurassic in Longtoushan of Zhenfeng, Guizhou, and its geological signifcance. *Guizhou Geol.* **1997**, *14*, 201–203. (In Chinese)

20. GXBGMR (Guangxi Bureau of Geology and Mineral Resources). *Regional Geology of Guangxi*; Geological Publishing House: Beijing, China, 1985; pp. 1–853. (In Chinese)

21. Liu, S.; Su, W.; Hu, R.; Feng, C.; Gao, S.; Coulson, I.M.; Wang, T.; Feng, G.; Tao, Y.; Xia, Y. Geochronological and geochemical constraints on the petrogenesis of alkaline ultramafic dykes from southwest Guizhou Province, SW China. *Lithos* **2010**, *114*, 253–264. [CrossRef]

22. Duan, L.; Meng, Q.R.; Christie-Blick, N.; Wu, G.L. New insights on the Triassic tectonic development of South China from the detrital zircon provenance of Nanpanjiang turbidites. *Geol. Soc. Am. Bull.* **2018**, *130*, 24–34. [CrossRef]

23. Duan, L.; Meng, Q.R.; Wu, G.-L.; Yang, Z.; Wang, J.; Zhan, R. Nanpanjiang basin: A window on the tectonic development of south China during Triassic assembly of the southeastern and eastern Asia. *Gondwana Res.* **2020**, *78*, 189–209. [CrossRef]

24. Xu, W.; Liu, Y.P.G.; Guo, L.G.; Ye, L.N.; Pi, D.H.; Liao, Z.E. Geochemistry and tectonic setting of the Babu Ophiolite, Southeast Yunnan. *Acta Mineral. Sin.* **2008**, *28*, 6–14.

25. GXBGMR (Guangxi Bureau of Geology and Mineral Resources). *Geological Map and Report of Jingxi Sheet (F-48-11), Scale 1:200,000*; GXBGMR (Guangxi Bureau of Geology and Mineral Resources): Guilin, China, 1969; pp. 1–64. (In Chinese)

26. Hou, K.J.; Li, Y.H.; Tian, Y.R. In situ U–Pb zircon dating using laser ablation-multi ion counting-ICP-MS. *Miner. Depos.* **2009**, *28*, 481–492. (In Chinese)

27. Pu, W.; Gao, J.F.; Zhao, K.D.; Ling, H.; Jiang, S. Separation Method of Rb–Sr, Sm–Nd Using DCTA and HIBA. *J. Nanjing Univ.* **2005**, *41*, 445–450. (In Chinese)

28. Winchester, J.; Floyd, P. Geochemical discrimination of different magma series and their differentiation products using immobile elements. *Chem. Geol.* **1977**, *20*, 325–343. [CrossRef]

29. Sun, S.S.; McDonough, W.F. Chemical and isotopic systematics of oceanic basalts: Implications for mantle composition and processes. *Geol. Soc. Lond. Spec. Publ.* **1989**, *42*, 313–345. [CrossRef]

30. Espanon, V.R.; Chivas, A.R.; Kinsley, L.P.J.; Dosseto, A. Geochemical variations in the Quaternary Andean back-arc volcanism, southern Mendoza, Argentina. *Lithos* **2014**, *208–209*, 251–264. [CrossRef]

31. Hofmann, A. Mantle geochemistry: The message from oceanic volcanism. *Nature* **1997**, *385*, 219. [CrossRef]

32. Zindler, A.; Hart, S. Chemical geodynamics. *Annu. Rev. Earth Planet. Sci.* **1986**, *14*, 493–571. [CrossRef]

33. Zimmer, M.; Kroner, A.; Jochum, K.P.; Reischmann, T.; Todt, W. The Gabal-Gerf complex: A Precambrian N-MORB ophiolite in the Nubian Shield, NE Africa. *Chem. Geol.* **1995**, *123*, 29–51. [CrossRef]

34. Cen, T.; Li, W.X.; Wang, X.C.; Pang, C.J.; Li, Z.X.; Xing, G.F.; Zhao, X.L.; Tao, J.H. Petrogenesis of early Jurassic basalts in southern Jiangxi Province, South China: Implications for the thermal state of the Mesozoic mantle beneath South China. *Lithos* **2016**, *256*, 311–330. [CrossRef]

35. He, Z.Y.; Xu, X.S.; Niu, Y.L. Petrogenesis and tectonic significance of a Mesozoic granite–syenite–gabbro association from inland South China. *Lithos* **2010**, *119*, 621–641. [CrossRef]

36. Wang, Y.; Fan, W.; Peng, T.; Guo, F. Elemental and Sr–Nd isotopic systematics of the early Mesozoic volcanic sequence in southern Jiangxi Province, South China: Petrogenesis and tectonic implications. *Int. J. Earth Sci.* **2005**, *94*, 53–65. [CrossRef]

37. Li, X.H.; Chung, S.L.; Zhou, H.W.; Lo, C.H.; Liu, Y.; Chen, C.W. Jurassic intraplate magmatism in southern Hunan-eastern Guangxi: Ar-40/Ar-39 dating, geochemistry, Sr–Nd isotopes and implications for the tectonic evolution of SE China. *Geol. Soc. Lond. Spec. Publ.* **2004**, *226*, 193–215. [CrossRef]

38. Li, X.H.; Chen, Z.; Liu, D.Y.; Li, W.X. Jurassic gabbro-granite-syenite suites from Southern Jiangxi province, SE China: Age, origin, and tectonic significance. *Int. Geol. Rev.* **2003**, *45*, 898–921. [CrossRef]

39. Wang, Y.J.; Fan, W.M.; Guo, F.; Peng, T.P.; Li, C.W. Geochemistry of Mesozoic mafic rocks adjacent to the Chenzhou-Linwu fault, South China: Implications for the lithospheric boundary between the Yangtze and Cathaysia blocks. *Int. Geol. Rev.* **2003**, *45*, 263–286. [CrossRef]

40. Wood, D.A.; Joron, J.L.; Treuil, M. A re-appraisal of the use of trace elements to classify and discriminate between magma series erupted in different tectonic settings. *Earth Planet. Sci. Lett.* **1979**, *45*, 326–336. [CrossRef]

41. Polat, A.; Hofmann, A.W. Alteration and geochemical patterns in the 3.7–3.8 Ga Isua greenstone belt, West Greenland. *Precambrian Res.* **2003**, *126*, 197–218. [CrossRef]

42. Polat, A.; Hofmann, A.W.; Rosing, M.T. Boninite-like volcanic rocks in the 3.7–3.8 Ga Isua greenstone belt, West Greenland: Geochemical evidence for intra-oceanic subduction zone processes in the early Earth. *Chem. Geol.* **2002**, *184*, 231–254. [CrossRef]

43. Rudnick, R.L.; Gao, S. Composition of the continental crust. *Treatise Geochem.* **2003**, *3*, 659.

44. Hofmann, A.W.; Jochum, K.P.; Seufert, M.; White, W.M. Nb and Pb in oceanic basalts: New constraints on mantle evolution. *Earth Planet. Sci. Lett.* **1986**, *79*, 33–45. [CrossRef]

45. Weaver, B.L. The origin of ocean island basalt end-member compositions: Trace element and isotopic constraints. *Earth Planet. Sci. Lett.* **1991**, *104*, 381–397. [CrossRef]

46. Thompson, R.N.; Morrison, M.A. Asthenospheric and lower-lithospheric mantle contributions to continental extensional magmatism: An example from the British Tertiary Province. *Chem. Geol.* **1988**, *68*, 1–15. [CrossRef]

47. Fitton, J.G.; James, D.; Kempton, P.D.; Ormerod, D.S.; Leeman, W.P. The Role of Lithospheric Mantle in the Generation of Late Cenozoic Basic Magmas in the Western United States. *J. Pet. Spec.* **1988**, *1*, 331–349. [CrossRef]

48. Yang, J.H.; Sun, J.F.; Chen, F.K.; Wilde, S.A.; Wu, F.Y. Sources and Petrogenesis of Late Triassic Dolerite Dikes in the Liaodong Peninsula: Implications for Post-collisional Lithosphere Thinning of the Eastern North China Craton. *J. Petrol.* **2007**, *48*, 1973–1997. [CrossRef]

49. Aldanmaz, E.; Pearce, J.A.; Thirlwall, M.F.; Mitchell, J.G. Petrogenetic evolution of late Cenozoic, post-collision volcanism in western Anatolia, Turkey. *J. Volcanol. Geotherm. Res.* **2000**, *102*, 67–95. [CrossRef]

50. Xu, Y.G.; Ma, J.L.; Frey, F.A.; Feigenson, M.D.; Liu, J.F. Role of lithosphere–asthenosphere interaction in the genesis of Quaternary alkali and tholeiitic basalts from Datong, western North China Craton. *Chem. Geol.* **2005**, *224*, 247–271. [CrossRef]

51. Shaw, D.M. Trace element fractionation during anatexis. *Geochim. Cosmochim. Acta* **1970**, *34*, 237–243. [CrossRef]

52. Johnson, K.T.M. Experimental determination of partition coefficients for rare earth and high-field-strength elements between clinopyroxene, garnet, and basaltic melt at high pressures. *Contrib. Mineral. Petrol.* **1998**, *133*, 60–68. [CrossRef]

53. Xu, Y.G.; Chung, S.L.; Jahn, B.M.; Wu, G.Y. Petrologic and geochemical constraints on the petrogenesis of Permian–Triassic Emeishan flood basalts in southwestern China. *Lithos* **2001**, *58*, 145–168. [CrossRef]

54. Kay, R.W.; Kay, S.M. Delamination and delamination magmatism. *Tectonophysics* **1993**, *219*, 177–189. [CrossRef]

55. Bonin, B. Do coeval mafic and felsic magmas in post-collisional to within-plate regimes necessarily imply two contrasting, mantle and crustal, sources? A review. *Lithos* **2004**, *78*, 1–24. [CrossRef]

56. Søager, N.; Holm, P.M.; Llambías, E.J. Payenia volcanic province, southern Mendoza, Argentina: OIB mantle upwelling in a backarc environment. *Chem. Geol.* **2013**, *349*, 36–53. [CrossRef]

57. Qiu, L.; Yang, W.X.; Yan, D.P.; Wells, M.L.; Qiu, J.T.; Gao, T.; Dong, J.M.; Zhang, L.L.; Wang, F.Y. Geochronology of early Mesozoic diabase units in southwestern China: Metallogenic and tectonic implications. *Geol. Mag.* **2019**, *156*, 1141–1156. [CrossRef]

58. Zhong, Y.T.; He, B.; Mundil, R.; Xu, Y.G. CA-TIMS zircon U–Pb dating of felsic ignimbrite from the Binchuan section: Implications for the termination age of Emeishan large igneous province. *Lithos* **2014**, *204*, 14–19. [CrossRef]

59. He, B.; Xu, Y.G.; Huang, X.L.; Luo, Z.Y.; Shi, Y.R.; Yang, Q.J.; Yu, S.Y. Age and duration of the Emeishan flood volcanism, SW China: Geochemistry and SHRIMP zircon U–Pb dating of silicic ignimbrites, post-volcanic Xuanwei Formation and clay tuff at the Chaotian section. *Earth Planet. Sci. Lett.* **2007**, *255*, 306–323. [CrossRef]

60. Dilek, Y.; Altunkaynak, Ş. Cenozoic Crustal Evolution and Mantle Dynamics of Post-Collisional Magmatism in Western Anatolia. *Int. Geol. Rev.* **2007**, *49*, 431–453. [CrossRef]

61. Bonin, B.L.; Azzouni-Sekkal, A.; Bussy, F.; Ferrag, S. Alkali-calcic and alkaline post-orogenic (PO) granite magmatism: Petrologic constraints and geodynamic settings. *Lithos* **1998**, *45*, 45–70. [CrossRef]

62. Floyd, P.A.; Kelling, G.; Gokcen, S.L.; Gokcen, N. Geochemistry and tectonic environment of basaltic rocks from the Misis ophiolitic mélange, south Turkey. *Chem. Geol.* **1991**, *89*, 263–279. [CrossRef]

63. Shuto, K.; Ishimoto, H.; Hirahara, Y.; Sato, M.; Matsui, K.; Fujibayashi, N.; Takazawa, E.; Yabuki, K.; Sekine, M.; Kato, M.; et al. Geochemical secular variation of magma source during Early to Middle Miocene time in the Niigata area, NE Japan: Asthenospheric mantle upwelling during back-arc basin opening. *Lithos* **2006**, *86*, 1–33. [CrossRef]

64. Woodhead, J.; Eggins, S.; Gamble, J. High field strength and transition element systematics in island arc and back-arc basin basalts: Evidence for multi-phase melt extraction and a depleted mantle wedge. *Earth Planet. Sci. Lett.* **1993**, *114*, 491–504. [CrossRef]

65. Pearce, J.A. Immobile element fingerprinting of ophiolites. *Elements* **2014**, *10*, 101–108. [CrossRef]

66. Li, X.H.; Li, Z.X.; He, B.; Li, W.X.; Li, Q.L.; Gao, Y.; Wang, X.C. The Early Permian active continental margin and crustal growth of the Cathaysia Block: In situ U–Pb, Lu–Hf and O isotope analyses of detrital zircons. *Chem. Geol.* **2012**, *328*, 195–207. [CrossRef]

67. Li, X.H.; Li, Z.X.; Li, W.X.; Wang, Y. Initiation of the Indosinian Orogeny in South China: Evidence for a Permian Magmatic Arc on Hainan Island. *J. Geol.* **2006**, *114*, 341–353. [CrossRef]

68. Xu, C.H.; Zhang, L.; Shi, H.S.; Brix, M.R.; Huhma, H.; Chen, L.H.; Zhang, M.Q.; Zhou, Z.Y. Tracing an Early Jurassic magmatic arc from South to East China Seas. *Tectonics* **2017**, *36*, 466–492. [CrossRef]

69. Yuan, W.; Yang, Z.Y.; Zhao, X.X.; Santosh, M.; Zhou, X.J. Early Jurassic granitoids from deep drill holes in the East China Sea Basin: Implications for the initiation of Palaeo-Pacific tectono-magmatic cycle. *Int. Geol. Rev.* **2018**, *60*, 813–824. [CrossRef]

70. Yui, T.F.; Chu, H.T.; Suga, K.; Lan, C.Y.; Chung, S.H.; Wang, K.L.; Grove, M. Subduction-related 200 Ma Talun metagranite, SE Taiwan: An age constraint for palaeo-Pacific plate subduction beneath South China Block during the Mesozoic. *Int. Geol. Rev.* **2017**, *59*, 333–346. [CrossRef]

71. Faure, M.; Ishida, K. The Mid-Upper Jurassic olistostrome of the west Philippines: A distinctive key-marker for the North Palawan block. *J. Southeast Asian Earth Sci.* **1990**, *4*, 61–67. [CrossRef]

72. Isozaki, Y. Jurassic accretion tectonics of Japan. *Isl. Arc* **1997**, *6*, 25–51. [CrossRef]

73. Wakita, K.; Metcalfe, I. Ocean plate stratigraphy in East and Southeast Asia. *J. Asian Earth Sci.* **2005**, *24*, 679–702. [CrossRef]

74. Yui, T.F.; Maki, K.; Lan, C.Y.; Hirata, T.; Chu, H.T.; Kon, Y.; Yokoyama, T.D.; Jahn, B.M.; Ernst, W.G. Detrital zircons from the Tananao metamorphic complex of Taiwan: Implications for sediment provenance and Mesozoic tectonics. *Tectonophysics* **2012**, *541*, 31–42. [CrossRef]

75. Chen, M.H.; Mao, J.W.; Qu, W.J.; Wu, L.L.; Phillip, J.U.; Tony, N.; Zheng, J.M.; Qin, Y.Z. Re-Os Dating of Arsenian Pyrites from the Lannigou Gold Deposit, Zhenfeng, Guizhou Province, and Its Geological Significances. *Geol. Rev.* **2007**, *53*, 371–382. (In Chinese)

76. Chen, M.H.; Huang, Q.W.; Hu, Y.; Chen, Z.Y.; Zhang, W. Genetic Types of Phyllosilicate (Micas) and Its $^{39}$Ar–$^{40}$Ar Dating in Lannigou Gold Deposit, Guizhou Province, China. *Acta Mineral. Sin.* **2009**, *29*, 353–362. (In Chinese)

77. Muntean, J.L.; Cline, J.S.; Simon, A.C.; Longo, A.A. Magmatic–hydrothermal origin of Nevada's Carlin-type gold deposits. *Nat. Geosci.* **2011**, *4*, 122–127. [CrossRef]

78. Emsbo, P.; Groves, D.I.; Hofstra, A.H.; Bierlein, F.P. The giant Carlin gold province: A protracted interplay of orogenic, basinal, and hydrothermal processes above a lithospheric boundary. *Min. Depos.* **2006**, *41*, 517–525. [CrossRef]